arXiv:1909.08214v1 [cond-mat.mtrl-sci] 18 Sep 2019

# Disentangling the effects of doping, strain and defects in monolayer $WS_2$ by optical spectroscopy

Pavel V. Kolesnichenko,[†,¶] Qianhui Zhang,[‡] Changxi Zheng,[‡,§] Michael S. Fuhrer,[‡,§] and Jeffrey A. Davis[*,†,¶]

†*Centre for Quantum and Optical Science, Swinburne University of Technology, Melbourne, Victoria 3122, Australia*

‡*Monash University, Melbourne, Victoria 3800, Australia*

¶*ARC Centre of Excellence in Future Low-Energy Electronics Technologies, Swinburne University of Technology, Melbourne, Victoria 3122, Australia*

§*ARC Centre of Excellence in Future Low-Energy Electronics Technologies, Monash University, Victoria 3800 Australia*

E-mail: jdavis@swin.edu.au

**Abstract**

Monolayers of transition metal dichalcogenides (TMdC) are promising candidates for realization of a new generation of optoelectronic devices. The optical properties of these two-dimensional materials, however, vary from flake to flake, or even across individual flakes, and change over time, all of which makes control of the optoelectronic properties challenging. There are many different perturbations that can alter the optical properties, including charge doping, defects, strain, oxidation, and water intercalation. Identifying which perturbations are present is usually not straightforward and requires

multiple measurements using multiple experimental modalities, which presents barriers when attempting to optimise preparation of these materials. Here, we apply high-resolution photoluminescence and differential reflectance hyperspectral imaging *in situ* to CVD-grown $WS_2$ monolayers. By combining these two optical measurements and using a statistical correlation analysis we are able to disentangle three contributions modulating optoelectronic properties of these materials: electron doping, strain and defects. In separating these contributions, we also observe that the B-exciton energy is less sensitive to variations in doping density than A-excitons.

# Introduction

For more than a decade two-dimensional (2D) transition metal dichalcogenides (TMdCs) have been extensively studied as they offer unprecedented physics not achievable in conventional semiconducting quantum wells. The peculiar combination of their crystal structure without inversion symmetry;[1,2] strong spin-orbit (SO) interactions originating from the heavy transition metal elements;[2] and the time-reversal symmetry acting to lock spin and valley degrees of freedom makes these materials ideal platforms for realization of valley-selective[3] and spin-polarized[4] optoelectronics. Owing to their monolayer nature, the optoelectronic properties of these materials are governed by excitonic effects that are greatly enhanced compared to conventional semiconducting quantum wells.[5] Several conceptual devices based on 2D materials, such as field-effect transistor,[6] memory cells,[7,8] *p*-*n* junction[9] and photodiodes[10,11] have been already demonstrated to have the potential to outperform their conventional analogs.

However, the majority of the demonstrated devices are based on "one-off" prototypes based on mechanically exfoliated monolayers[6–8,10,11] and their fabrication lacks scalability. Chemical vapour deposition (CVD) is promising for massive industrialization of novel optoelectronic devices, but, as it currently stands, monolayers grown via CVD are randomly distributed across their supporting substrates with each monolayer flake having heteroge-

neous optoelectronic properties. These heterogeneities are often challenging to interpret as the crystal structure can be subject to a complex perturbation resulting from strain,[12] defects,[13–17] grain boundaries[17–22] as well as oxidation,[19] water intercalation[23] and other aging processes.[24] Despite this variability and complexity, CVD approaches commonly result in triangular monolayers with variations in the optical properties that are also trigonally-symmetric.[13–17,20–22,24–32] Most simply, these correspond to regions of brighter (bright regions) and darker (dark regions) photoluminescence (PL) emission. The dark regions have been commonly attributed to intra-flake grain boundaries,[17,20,21] structural or chemical heterogeneities,[14,15,25,26,31,32] and/or linked to increases in $n$-doping. Identifying the specific perturbation or combination of them is challenging, and the details will vary depending on the specifics of the growth, substrate, environment and history of the monolayer.

Disentangling various contributions modulating optoelectronic properties of TMdC monolayers usually requires complementary and often complicated methods. These can include optical and Raman spectroscopy, atomic force microscopy (AFM), Kelvin probe force microscopy (KPFM), and photoemission spectroscopy, amongst others. While all these methods have their own advantages they usually require repositioning of the monolayer from one experimental setting to another.

Here we demonstrate the ability to disentangle the effects of doping, strain and defects, which play a major role in shaping the optoelectronic properties of TMdC monolayers, using solely optical spectroscopy measurements. To acheive this we record PL and absorption hyperspectral images of $WS_2$ monolayers grown via CVD with high spatial resolution ($\sim$300–380 nm). Among the countless reports showing spatial maps of PL spectral characteristics of TMdC monolayers, only few presented spatially resolved absorption characteristics,[22,30,33–37] and even fewer with the spatial resolution less than 500 nm.[33,35–37] Having both emission and absorption hyperspectral maps provides a greater level of detail and allows parameters such as PL Stokes shift and PL quantum yield to be determined, which help to identify the different perturbations. To analyse the large amount of data, we extract different spectral

properties (including peak amplitude, wavelength and width for A-excitons, B-excitons, and trions) from each point in space and perform a correlation analysis which ultimately allows us to disentangle the effects of strain, doping and disorder. This idea of correlating different spectral properties to better understand 2D materials has previously been shown to provide useful insights when applied to Raman and PL spectroscopy measurements on graphene,[38] TMdC monolayers[12,17,20,39] and their heterostructures.[40] We show here that correlating PL and absorption measurements can provide similar insights into the properties and pertubations of 2D materials.

## Results and discussion

We examine two monolayer $WS_2$ flakes grown by CVD on sapphire with properties that encompass the range of observed behaviours. The results for a further five flakes are shown in the Supporting Information. The PL hyperspectral images were obtained by illuminating the sample with a 410 nm cw laser and collecting the emission with a 100x objective in a modified confocal microscope as detailed in the Experimental section.

Figure 1a maps the integrated PL intensity across flake #1, revealing a commonly observed trigonally-symmetric pattern. In the interior these are categorised broadly as (i) *dark regions*, and (ii) *bright regions*. At the edges of the flake the brightest PL is observed and defines a third domain. These bright edges have been commonly observed for TMdC monolayers on hydrophilic substrates such as sapphire.[23] In these regions water intercalation[23] and interaction of sulphur (S) vacancies with environmental molecules[41–44] reduces the intrinsic $n$-doping levels commonly found in these materials resulting in a brighter PL emission. Here, we focus on the interior of $WS_2$ monolayers and will omit further discussion of edges.

The integrated and normalized PL spectra from the dark and bright regions are shown in Figure 1f. The asymmetric spectral shape of the PL spectra is typical for CVD-grown $WS_2$ monolayers and arises from the dominant emission from the A exciton, with the low energy

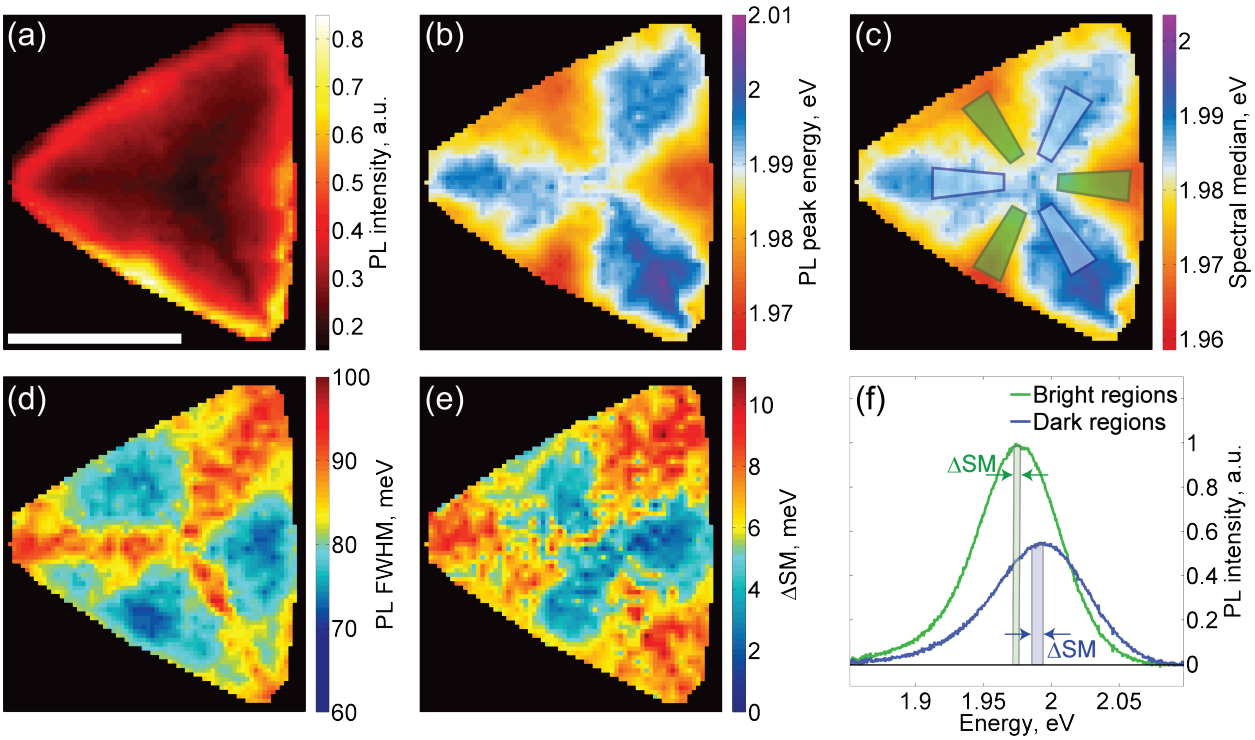



Figure 1: Flake #1: PL spatial maps of (a) normalized integrated intensity, (b) peak energy, (c) spectral median, (d) FWHM, and (e) ΔSM. (f) Normalized integrated PL spectra across the dark (blue) and bright (green) regions. The spectra are normalized to the peak intensity of PL spectrum integrated across the bright regions. The corresponding integration areas are shown in (c). The length of the scalebar in (a) corresponds to 10 $\mu$m.

tail coming from trions and/or defect states. To further investigate the spatial variation across the flake, PL peak energy (Figure 1b), spectral median (SM) (Figure 1c), and PL FWHM (Figure 1d) were mapped across the sample. These spatial maps show that the PL emission from the dark regions is blue-shifted (Figure 1b) and broadened (Figure 1d) compared to that from the bright regions. The SM is similar to the peak wavelength and is defined as the energy that splits the PL spectral profile into two equal contributions such that the total spectral weight to the left of the SM is equal to the spectral weight to the right of the SM. In contrast to the peak energy, however, the SM is sensitive to changes in the asymmetry of the peak and thus changes to the trion contribution. To highlight the difference, we also plot ΔSM - the difference between the SM and the peak energy (Figure 1e). The value of ΔSM (Figure 1e) is predominantly defined by the charging energy (CE) of a

trion (see Supporting Information) and represents a good, fit-free, indication of how the CE varies across the flake. As seen from Figure 1e,f, the value of $\Delta$SM (and, therefore, CE) is larger in the dark regions, which suggests that the doping density may be higher in these regions, which would also lead to the reduced emission intensity observed.[45] However, there are also other mechanisms that could explain the variations of the PL emission properties across the flake. For example, the weaker, blue-shifted, and broadened PL in the dark regions could originate from intra-flake grain boundaries.[17,20,21,46] On the other hand, the increase in intensity and red-shift in the bright regions could be due to environmental molecules interacting with S-vacancies, which is known to increase the PL quantum yield (QY).[41–44] Tensile strain has also been shown to lower emission energy[47–50] and alter the exciton-phonon coupling with the effect of narrowing the A-exciton linewidth.[51,52] The presence of tensile strain in the bright regions has been reported previously for CVD-grown monolayers with similar trigonal-symmetric patterns.[28,53]

From these PL maps it is evident that the integrated intensity, peak energy, FWHM and CE appear to be strongly correlated and vary together across the flake. These variations could be due to gradually changing strain, defect density, doping density or grain boundaries. In order to differentiate between these possibilities, we correlate these PL maps with absorption maps.

We obtain spatially-resolved absorption spectra of $WS_2$ monolayers (Figure 2) by differential reflectance (DR) hyperspectral imaging and use the approximation that DR is proportional to the absorption coefficient.[54] This is a reasonable approximation for the case of monolayers of $WS_2$ on a thick sapphire substrate, where interference effects are minor[30] and are nearly absent in the spectral range of the A-exciton absorption peak.[55] Figure 2a shows the DR spectra integrated over the same areas (shown in inset) as in the case of the corresponding PL spectra considered above. The measured DR spectra consist of the three prominent features. The A- and B-exciton transitions originate from the SO split valence and conduction bands at K symmetry points in the first Brillouin zone, whereas the onset

of the third peak belongs to the C-exciton transitions in the band-nesting region.[56]

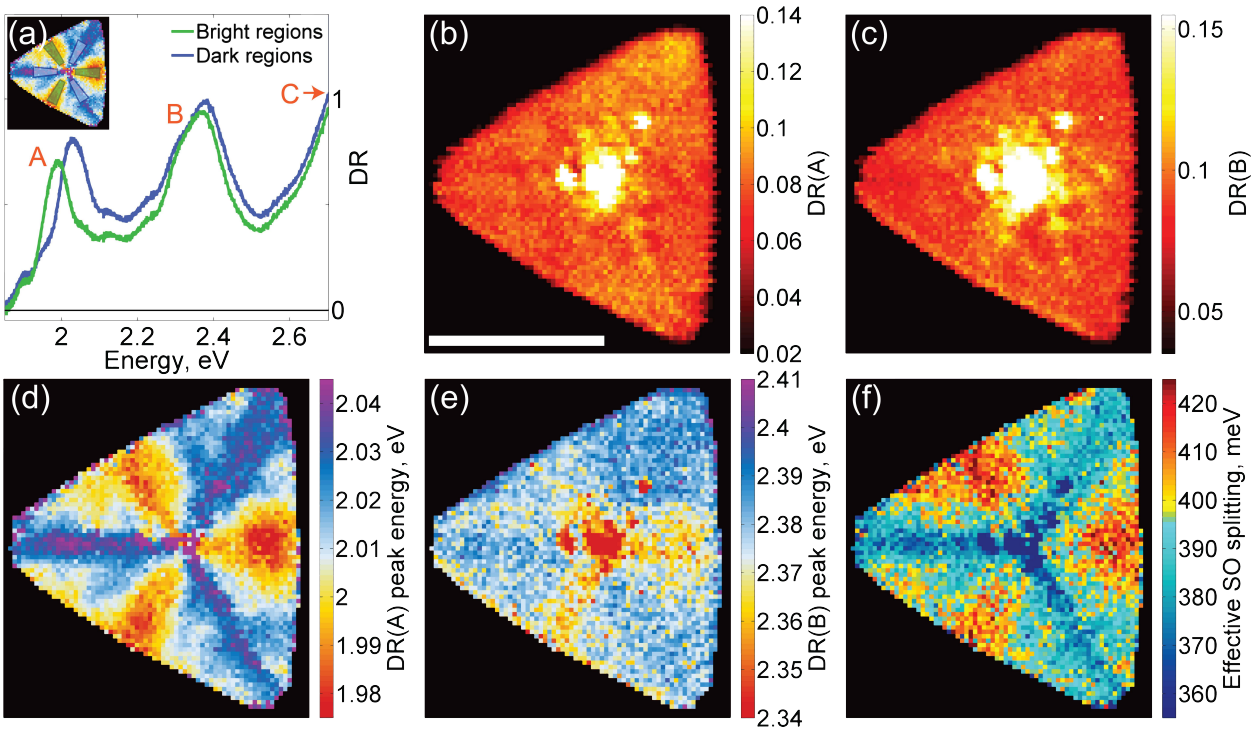



Figure 2: Flake #1: comparison of A- and B-exciton spectral characteristics. (a) DR spectra integrated over the dark (blue) and bright (green) regions shown in inset. Spatial maps of DR peak amplitude of (b) A- and (c) B-exciton transition; (d) A- and (e) B-exciton transition energies, and (f) effective SO. The length of the scalebar in (b) corresponds to 10 $\mu$m.

The spatial maps of the A- and B-exciton absorption features (Figure 2) show that in contrast to PL, the absorption amplitudes of these two peaks (Figure 2b,c) show only minor variations across the monolayer. This suggests that the oscillator strength is not significantly changed, but rather that the changes in PL intensity are due to reduced PL QY. The bright regions near the centre of the triangles correspond to multilayers which typically give a greater reflectance contrast.[33,35] These multilayer regions are not so evident in the PL maps because the PL from multilayers is reduced and these regions lie in areas where the PL intensity is already low.

The A-exciton absorption peak energy (Figure 2d) varies significantly between the dark and bright regions, similar to the PL emission. In contrast, the B-exciton energy varies by a much smaller amount (Figure 2e). This is also clear in the integrated DR plots in Figure 2a

and was observed for all flakes examined in this work (see Supplementary Material). This results in spatial variations of the effective SO splitting shown in Figure 2f which could arise due to changes in the valence band SO-splitting, the conduction band SO-splitting, variations in the Fermi energy or any combination thereof. Before addressing this question, we first consider further the properties of the A-exciton.

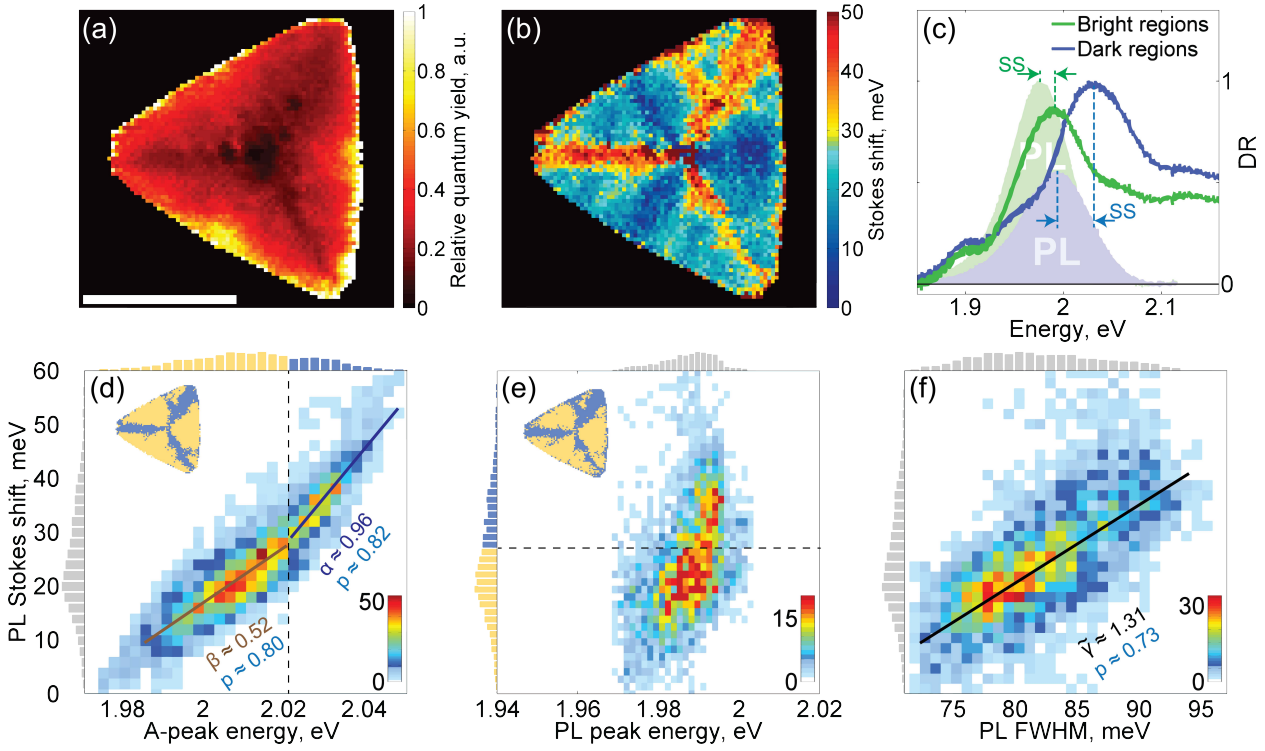



Figure 3: (a) Relative PL quantum yield and (b) PL Stokes shift for the flake #1. (c) DR and PL spectra integrated over the areas shown in inset in Figure 2a. Comparison of correlation plots (2D histograms) of PL Stokes shift versus A-exciton DR peak energy (d), PL peak energy (e) and PL FWHM (f). The bin size in (d) is 0.003×2.012 eV·meV, in (e) is 0.001×1.391 eV·meV, and in (f) is 0.84×1.89 meV·meV. Horizontally and vertically integrated histograms are shown on the left and on the top of each plot in (d–f), respectively. The integrated 1D correlation plots in (d,e) were split into two parts corresponding to dark (blue) and bright (yellow) regions. In (b) it was not possible to find a vertical boundary, therefore a horizontal boundary was used instead. All boundaries were drawn from where the slope of a chosen 1D histogram changes. The data points from each side of a boundary were mapped back onto the corresponding flake (see insets in (d,e)). In (d) the two data sets corresponding to dark and bright regions were fit with linear functions. In (f) data set was fit with a single linear function. For all linear fits the extracted slopes and calculated Pearson's correlation coefficients are given. Colorbars in (d–f) reflect the number of data points within a bin. The length of the scalebar in (a) corresponds to 10 $\mu$m.

Figure 3a,b combines the PL and DR maps discussed above to reconstruct the spatial variations of the relative PL QY and PL Stokes shift of monolayer flake #1. The spatial maps of PL QY (Figure 3a) highlight that the reduction of PL intensity in the dark regions is primarily due to the lower PL QY. This could arise due to higher $n$-doping levels and/or greater defect density in the dark regions.[18,45,57] The map of PL Stokes shift (Figure 3b) shows values ranging from ∼5 meV in the bright regions to ∼55 meV in the dark regions. Integrated PL and absorption spectra in the dark and bright regions are superimposed in Figure 3c and show that the larger Stokes shift in the dark regions arises due to a large shift of the absorption peak.

In general, PL Stokes shift can originate from randomly-distributed disorder potentials and interactions with optical phonons[58,59] (Figure 4a), elevated electron doping density[45,60,61] (Figure 4b), or the presence of lattice strain field[52,62] (Figure 4c). To be more specific, it has been shown that there is a linear correlation of the PL Stokes shift with $n$-doping,[45] the amount of strain,[52] and disorder-induced PL spectral width ($\mathrm{FWHM_{disorder}}$).[58] In the case of increased $n$-doping, the increasing Fermi energy level in the conduction band results in the A-exciton absorption peak being blue-shifted, while the PL peak energy is relatively unchanged. This occurs because the absorption process drives transitions between the top of the valence band and the Fermi edge in the conduction band, whereas the emission is from states at the bottom of the conduction band; therefore the doping contribution to PL Stokes shift varies approximately linearly with the A-exciton absorption peak energy ($E_A$). Tensile strain results in a red-shift of the conduction band minimum at K symmetry points leading to a red-shift of both absorption and emission peak energies with similar but not equal shift rates. The absorption energy shifts faster than the emission, leading to a Stokes shift that decreases with increasing tensile strain.[52,63] Finally, the contribution from disorder can cause a change in the Stokes shift, with minimal change in absorption energy. The Stokes shift due to disorder will, however, be linearly correlated with the FWHM of the PL peak.[58]

To disentangle these different effects, we perform a statistical analysis correlating PL

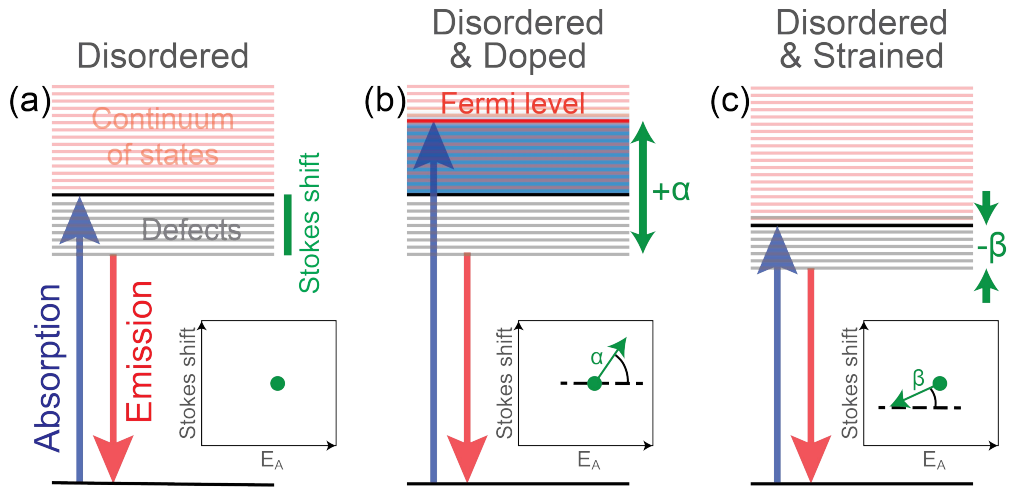



Figure 4: Schematic energy level diagrams showing absorption and emission processes resulting in finite PL Stokes shifts (green). (a) The case of undoped and unstrained monolayer with disorder. (b) The case of doped monolayer with disorder; the Fermi level is denoted by the red line; free electron states are shaded in blue; PL Stokes shift increases with the rate $+\alpha$. (c) The case of strained monolayer with disorder; PL Stokes shift decreases with the rate $-\beta$; both absorption and emission exhibit redshifts. Absorption (blue arrows) and emission (red arrows) energies, defect states (light grey) and continuum of states (light red) are denoted correspondingly.

Stokes shift with A-exciton absorption peak energy (Figure 3d), PL emission peak energy (Figure 3e) and PL FWHM (Figure 3f). Such correlation analyses have been shown previously to be powerful in separating physically distinct domains within $MoS_2$ monolayers[17,20] (using PL-Raman and PL-KPFM correlations), and disentangling the effects of strain and doping in graphene,[38] $MoS_2$ monolayers[39] and graphene/$MoS_2$ heterostructures[40] (using PL-Raman and Raman-Raman correlations). The plots shown in Fig. 3(d-f) are 2D histograms providing a basic idea of the data density while visually enhancing the clarity of trends within the overall scattered data. Each 2D histogram was integrated along the horizontal and vertical axes and reduced to corresponding 1D histograms that can be used to estimate the boundary (dotted line) separating the different spatial regions.

The correlation plot in Figure 3d reveals two distinct regions with different slopes. The region with the steeper slope, and higher absorption energy, maps onto lines extending from the centre of the monolayer flake to the apexes. In this region of the correlation plot it is

clear that there is a strong correlation between the Stokes shift and absorption peak energy, which is fit with a slope $\alpha \sim 0.96$ and Pearson's correlation coefficient ($p$) of 0.82. The high strength of this correlation suggests that there is one dominant origin of the changing Stokes shift in this spatial region. In contrast, for the same range of Stokes shifts there is no significant correlation with PL peak energy (Figure 3e). This correlation of PL Stokes shift with absorption peak energy, but not with PL emission peak energy, strongly supports increased electron doping in the dark regions and, particularly, the narrower regions indicated in the insets of Figure 3, although we do not exclude the possible effects of minor compressive strain in the dark regions.[14,64]

Away from these narrow regions connecting the centre to the apexes (i.e. in the yellow regions in the inset of Figure 3d), the slope of the correlation between Stokes shift and A-exciton absorption peak energy is reduced to $\beta \sim 0.52$ and the strength of the correlation is also slightly reduced, with the Pearson's correlation coefficient down to 0.8. In addition, a weak correlation between Stokes shift and PL peak energy is evident (Figure 3e). This matches well with strain-dependent studies[52,63] showing that with increasing strain both absorption and emission energies red-shift, with the rate of absorption peak energy shift being larger than that of the emission peak energy (Figure 4c). The net result is a Stokes shift that decreases with increasing strain, alongside a decrease in absorption energy and PL peak energy, as is the case in Figure 3d,e. We therefore suggest that in these regions, the doping density is reduced, and it is the variation of the tensile strain field that is primarily responsible for the changes in absorption energy, PL peak energy and Stokes shift in these regions. Although, we note that the Pearson's correlation coefficient is lower in this part of the correlation plots, which suggests a more significant contribution from other sources, possibly including disorder and a small contribution from electron doping. Returning to the maps of Stokes shift (Figure 3b), absorption energy (Figure 2d) and PL peak energy (Figure 1b), the changes to these spectral properties as a function of position then indicates that tensile strain increases from the lines-to-the-apexes to the centres of the sides. This

also explains why the two distinct slopes meet at the end of their ranges, and the trend in the correlation data varies continuously: the highly doped regions (along the lines to the apexes) occur at the regions with lowest tensile strain.

Further insight into the role of disorder in the Stokes shift and overall optical properties can be gained from the correlation between the Stokes shift and the FWHM of the PL peak, as shown in Figure 3f. It has been previously reported that the contribution solely from disordered potential should result in a linear trend between the PL Stokes shift and exciton PL emission width with a definite slope of $\sim$0.55.[58] The slope measured in Figure 3f is $\sim$1.31, which is much steeper (i.e. the Stokes shift increases faster than expected from just disorder induced broadening) and indicates that the PL Stokes shift in this flake is affected primarily by doping and strain. That is, the larger $n$-doping density in the dark regions broadens PL emission and the increasing tensile strain in the bright regions narrows the PL linewidth.[51,52]

From these measurements we can therefore make the following conclusions regarding the perturbations of this flake: along the lines from the centre to the apexes, there is an elevated (and varying) $n$-doping density. Away from these lines the doping density gradually decreases and tensile strain begins to take over as the dominant factor affecting the optical properties. In this sample random defects and disorder make only minimal impact on the optical properties compared to doping and strain.

Returning to the B-exciton, Fig. 2(e), the much smaller variation in absorption energy follows a similar pattern to, and correlates with, the PL peak energy. This variation is thus attributed to the changing strain across the flake. However, the absence of a substantially blue shifted region along the lines to the apex, as is seen for the A-exciton absorption (Figure 2d), indicates that the B-exciton energy is not significantly impacted by $n$-doping. Intuitively, this could be due to the conduction band involved in the B-exciton transition lying above the one involving the A-exciton transition, but in $WS_2$, this is not expected to be the case.[65] Alternatively, it could be due to competing influences cancelling out: for example, the predicted increase in SO splitting in the conduction band with increasing $n$-

doping[66] could offset the increase in Fermi energy. This remains an interesting question and the topic of further work.

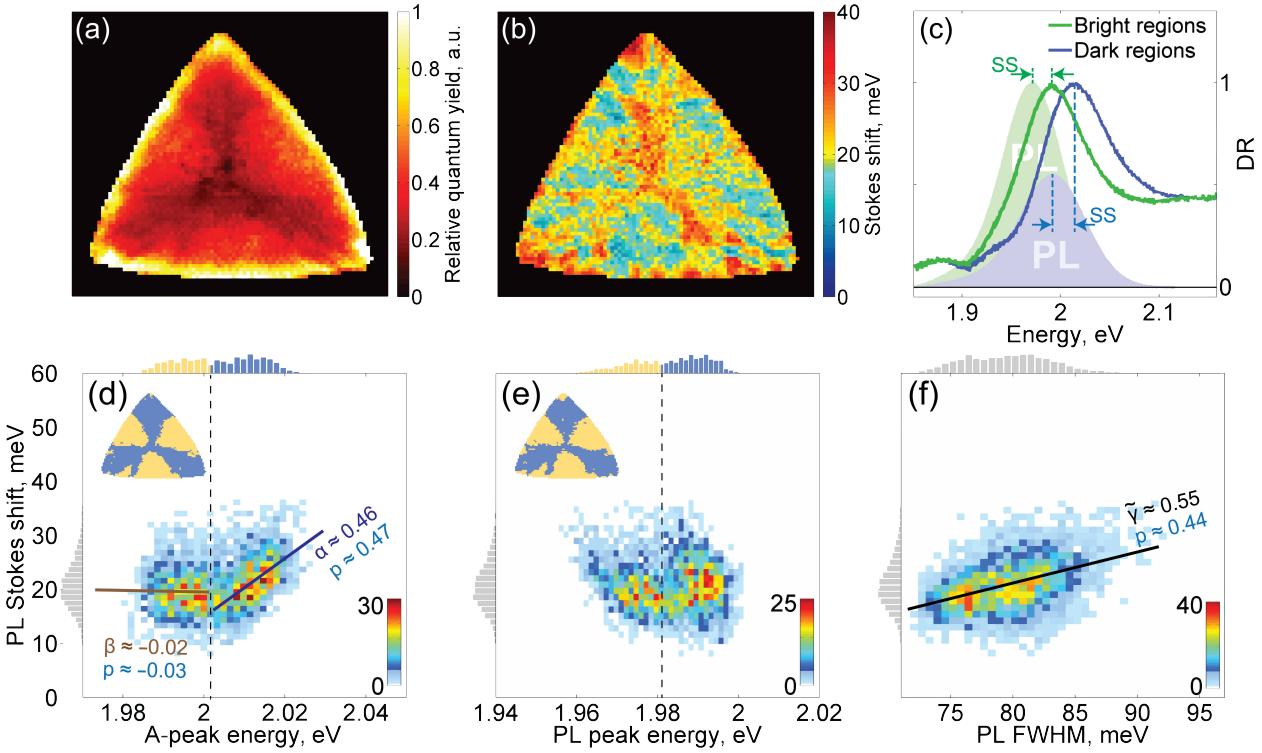



Figure 5: (a) Relative PL quantum yield and (b) PL Stokes shift for the flake #2. (c) DR and PL spectra integrated over the areas shown in Supporting Information. Comparison of correlation plots (2D histograms) of PL Stokes shift versus (d) A-exciton DR peak energy, (e) PL peak energy and (f) PL FWHM. The bin size in (d) is 0.02×1.56 eV·meV, in (e) is 0.02×1.63 eV·meV, and in (f) is 0.62×1.31 meV·meV. Horizontally and vertically integrated histograms are shown on the left and on the top of each plot in (d–f), respectively. The integrated 1D correlation plots in (d,e) were split into two parts corresponding to dark (blue) and bright (yellow) regions. All boundaries were drawn from where the slope of a chosen 1D histogram changes. The data points from each side of a boundary were mapped back onto the corresponding flake (see insets in (d,e)). In (d) the two data sets corresponding to dark and bright regions were fit with linear functions. In (f) data set was fit with a single linear function. For all linear fits the extracted slopes and calculated Pearson's correlation coefficients are given. Colorbars in (d–f) reflect the number of data points within a bin. The length of the scalebar in (a) corresponds to 10 $\mu$m.

To further demonstrate the capability of this approach that correlates PL and absorption imaging data we applied it to several other flakes, as shown in the Supporting Information. All other flakes examined in this work show similar trends, with two different slopes in the Stokes shift versus A-exciton absorption energy plot, and with the steeper slope, corre-

sponding to the darker regions. The trends in the flake with behaviour furthest from the one discussed so far (flake #2) are shown in Figure 5. In this case, the variation in PL QY is similar to that for flake #1, however, the PL Stokes shift only varies between ∼10 meV and ∼30 meV and does not exhibit the pronounced trigonal symmetry. (Refer to Supporting Information for PL and DR maps of flake #2.) One of the differences in the preparation of the flake #2 was that the measurements were performed after it had been exposed to air for more than four weeks after growth, compared to less than one week for flake #1. It has been shown previously that "aging" of monolayer flakes is accompanied by interactions with environmental molecules,[19,24] leading to changes in the doping density and increased disorder, while relaxation of the monolayer on the substrate can lead to reduced strain (e.g. via propagation of micro-cracks[24,67–69]). The clearest sign of aging, however, is that this flake has a much thicker edge region, with brighter PL, arising from water intercalation, which occurs over time.[23]

Figure 5c shows integrated DR and PL spectra for flake #2 (see Supporting Information for integration areas for this flake) and reveals that the main difference between the two monolayers (flake #1 and flake #2) is the energy of A-exciton absorption peak in the dark regions: for the flake #1 the peak is significantly blue-shifted, whereas for flake #2 the shift is similar to the bright regions. This strongly suggests that the doping density is reduced in the dark regions of flake #2. Figure 5d, which plots Stokes shift as a function of absorption energy, does show that there are still two distinct regions with different slopes. However, both slopes are significantly smaller, and there is a larger spread of data points (lower $p$-value). In the dark regions, the value of PL Stokes shift changes with a slope of ∼0.46 ($p = 0.47$), almost half compared to the flake #1, while for the bright regions the Stokes shift is nearly constant ($p = 0.03$). We attribute this to the aging process. In particular, the structural differences that were present in the flake #1 and likely in the flake #2 remain, however, over time the adsorption of other molecules from the environment reduces the overall $n$-doping and increases the amount of disorder. The significant role of disorder is also supported by

the weak anti-correlation between the PL Stokes shift and PL peak energy: lower emission peak energies correspond to a larger PL Stokes shift due to the excitons interacting with optical phonons that assist the quasiparticles in finding deeper local minima of a fluctuating local potential.[58,59,70] In addition, Figure 5f shows the slope of the PL Stokes shift versus PL FWHM to be ∼0.55. This matches the case when a disordered potential is the primary cause for a non-zero PL Stokes shift[58] again supporting our conclusions that in this flake disorder induced through aging dominates the optical properties, albeit in the presence of strain and grain boundaries that were dominant in the freshly grown flake.

# Conclusions

We have investigated optoelectronic properties of $WS_2$ monolayers by correlating spatially distributed emission and absorption properties. The resultant ability to measure Stokes shift and PL quantum yield allowed us to better understand the different perturbations and their effect on the optical properties. Further insights were gained from correlation plots involving the Stokes shift, allowing us to identify (in freshly grown flakes) regions where the $n$-doping density is high (and varying), and regions where tensile strain is the dominant varying perturbation. In the case of the aged flake, we were able to identify the much greater role played by disorder, likely due to the interactions between the monolayer flake and its environment. The identification of regions with high $n$-doping density was supported by the introduction of ΔSM (the difference between the spectral median and the peak emission energy) as a reliable fitting-free estimation of the relative charging energy of trions, which varies with the doping density. In contrast, these measurements also revealed that the B-exciton energy is apparently unaffected by increased $n$-doping. While we discussed several possibilities further work is needed to understand the origin of this surprising effect.

Finally, the correlation plots that helped disentangle the different perturbations here represent just a small subset of the large multi-dimensional data-cube that is formed from

the spectral parameters obtained from the measured data. Development of other approaches to better breakdown this vast dataset may lead to further insights and even better capabilities to identify different types of perturbation in 2D materials.

# Experimental

## Sample preparation

The sample preparation was performed in a similar way as described in Ref. [71].

## Photoluminescence measurements

The spatially-resolved PL measurements were performed using the frames of an inverted microscope (Nikon Eclipse T*i*-U). Linearly polarized coherent excitation was provided by a cw laser diode (Thorlabs, L405P20, mounted into the TE-Cooled Mount TCLDM9, operated by a temperature controller TED200C and a laser diode controller LDC205C) tuned to the wavelength of ∼410 nm. The radiation is sent to a dichroic mirror reflecting wavelengths below and transmitting wavelengths above ∼593 nm. After the dichroic mirror, the laser is focused onto the sample by a 100x objective lens (Olympus) with numerical aperture NA=0.95. The power density at the sample was estimated to be ∼2.8 MW/cm$^2$. The induced PL from the samples is collected by the same objective lens (*epi*-fluorescence geometry) and is transmitted through the dichroic mirror and a lens (200 mm focal length). At the image plane of the lens, a pinhole of 150 $\mu$m diameter transmits the sample's region with ∼750 nm diameter. The signal transmitted through the pinhole is coupled to a multi-mode fiber (Avantes, 200 $\mu$m core diameter, 2 m length) by a free-space fiber coupler (Thorlabs, F810SMA-635). The fiber is attached to a spectrometer (Avantes, Avaspec-2048), and a 400 ms integration time was used at each point.

The sample was mounted on a dual-channel XY motorized translation stage (Applied Scientific Instrumentation, MS-2000), allowing for raster scanning mode. The scanning step

was chosen to be 250 nm (flakes #1,2,5,6,7) and 500 nm (flakes #3,4). The communication between the motorized stage and the spectrometer was established by means of a LabView code. All measurements have been performed at room temperature. The estimated spatial resolution of the setup is ∼300 nm (see Supporting Information).

### Differential reflectance measurements

The spatially-resolved DR measurements were performed using the same PL setup with only slight differences. Instead of the diode laser as an excitation source, a spectrally broad (∼400–800 nm) incoherent white light (CoolLED, *p*E-100) was directed to the sample via a 50:50 beam splitter. The brightness of white light allowed to use a pinhole of 100 $\mu$m diameter at the image plane transmitting a region of ∼500 nm diameter. The integration time was 150 ms. The resolution of the technique was estimated to be ∼380 nm at ∼620 nm excitation wavelength (see Supporting Information).

## Acknowledgement

This work was supported by the Australian Research Council Centre of Excellence for Future Low-Energy Electronics Technologies (CE170100039).

## Supporting Information Available

The following files are available free of charge.

The following files are available free of charge.

- Filename: acsnano_suppl_PK.pdf
- Filename: PL_SS_anim.avi

# References


1. Xiao, D.; Liu, G.-B.; Feng, W.; Xu, X.; Yao, W. Coupled Spin and Valley Physics in Monolayers of $MoS_2$ and Other Group-VI Dichalcogenides. *Physical Review Letters* **2012**, *108*, 196802.

2. Liu, G.-B.; Xiao, D.; Yao, Y.; Xu, X.; Yao, W. Electronic Structures and Theoretical Modelling of Two-Dimensional Group-VIB Transition Metal Dichalcogenides. *Chemical Society Reviews* **2015**, *44*, 2643–2663.

3. Schaibley, J. R.; Yu, H.; Clark, G.; Rivera, P.; Ross, J. S.; Seyler, K. L.; Yao, W.; Xu, X. Valleytronics in 2D Materials. *Nature Reviews Materials* **2016**, *1*, 16055.

4. Liu, W.; Xu, Y. *Spintronic 2D Materials: Fundamentals and Applications*; Elsevier, 2019.

5. Wang, G.; Chernikov, A.; Glazov, M. M.; Heinz, T. F.; Marie, X.; Amand, T.; Urbaszek, B. Colloquium : Excitons in Atomically Thin Transition Metal Dichalcogenides. *Reviews of Modern Physics* **2018**, *90*.

6. Georgiou, T.; Jalil, R.; Belle, B. D.; Britnell, L.; Gorbachev, R. V.; Morozov, S. V.; Kim, Y.-J.; Gholinia, A.; Haigh, S. J.; Makarovsky, O. *et al.* Vertical Field-Effect Transistor Based on Graphene–$WS_2$ Heterostructures for Flexible and Transparent Electronics. *Nature Nanotechnology* **2012**, *8*, 100–103.

7. Bertolazzi, S.; Krasnozhon, D.; Kis, A. Nonvolatile Memory Cells Based on $MoS_2$/Graphene Heterostructures. *ACS Nano* **2013**, *7*, 3246–3252.

8. Choi, M. S.; Lee, G.-H.; Yu, Y.-J.; Lee, D.-Y.; Lee, S. H.; Kim, P.; Hone, J.; Yoo, W. J. Controlled Charge Trapping by Molybdenum Disulphide and Graphene in Ultrathin Heterostructured Memory Devices. *Nature Communications* **2013**, *4*, 1624.

9. Deng, Y.; Luo, Z.; Conrad, N. J.; Liu, H.; Gong, Y.; Najmaei, S.; Ajayan, P. M.; Lou, J.; Xu, X.; Ye, P. D. Black Phosphorus–Monolayer $MoS_2$ van der Waals Heterojunction p–n Diode. *ACS Nano* **2014**, *8*, 8292–8299.

10. Furchi, M. M.; Pospischil, A.; Libisch, F.; BurgdÃűrfer, J.; Mueller, T. Photovoltaic Effect in an Electrically Tunable van der Waals Heterojunction. *Nano Letters* **2014**, *14*, 4785–4791.

11. Lee, C.-H.; Lee, G.-H.; van der Zande, A. M.; Chen, W.; Li, Y.; Han, M.; Cui, X.; Arefe, G.; Nuckolls, C.; Heinz, T. F. *et al.* Atomically Thin p–n Junctions with van der Waals Heterointerfaces. *Nature Nanotechnology* **2014**, *9*, 676–681.

12. Hsu, W.-T.; Lu, L.-S.; Wang, D.; Huang, J.-K.; Li, M.-Y.; Chang, T.-R.; Chou, Y.-C.; Juang, Z.-Y.; Jeng, H.-T.; Li, L.-J. *et al.* Evidence of Indirect Gap in Monolayer $WSe_2$. *Nature Communications* **2017**, *8*, 929.

13. Jeong, H. Y.; Lee, S. Y.; Ly, T. H.; Han, G. H.; Kim, H.; Nam, H.; Jiong, Z.; Shin, B. G.; Yun, S. J.; Kim, J. *et al.* Visualizing Point Defects in Transition-Metal Dichalcogenides Using Optical Microscopy. *ACS Nano* **2015**, *10*, 770–777.

14. Jeong, H. Y.; Jin, Y.; Yun, S. J.; Zhao, J.; Baik, J.; Keum, D. H.; Lee, H. S.; Lee, Y. H. Heterogeneous Defect Domains in Single-Crystalline Hexagonal $WS_2$. *Advanced Materials* **2017**, *29*, 1605043.

15. Lin, Y.-C.; Li, S.; Komsa, H.-P.; Chang, L.-J.; Krasheninnikov, A. V.; Eda, G.; Suenaga, K. Revealing the Atomic Defects of $WS_2$ Governing Its Distinct Optical Emissions. *Advanced Functional Materials* **2017**, *28*, 1704210.

16. Rosenberger, M. R.; Chuang, H.-J.; McCreary, K. M.; Li, C. H.; Jonker, B. T. Electrical Characterization of Discrete Defects and Impact of Defect Density on Photoluminescence in Monolayer $WS_2$. *ACS Nano* **2018**, *12*, 1793–1800.

17. Kastl, C.; Koch, R. J.; Chen, C. T.; Eichhorn, J.; Ulstrup, S.; Bostwick, A.; Jozwiak, C.; Kuykendall, T. R.; Borys, N. J.; Toma, F. M. *et al.* Effects of Defects on Band Structure and Excitons in $WS_2$ Revealed by Nanoscale Photoemission Spectroscopy. *ACS Nano* **2019**, *13*, 1284–1291.

18. van der Zande, A. M.; Huang, P. Y.; Chenet, D. A.; Berkelbach, T. C.; You, Y.; Lee, G.-H.; Heinz, T. F.; Reichman, D. R.; Muller, D. A.; Hone, J. C. Grains and grain boundaries in highly crystalline monolayer molybdenum disulphide. *Nature Materials* **2013**, *12*, 554–561.

19. Zhang, Y.; Zhang, Y.; Ji, Q.; Ju, J.; Yuan, H.; Shi, J.; Gao, T.; Ma, D.; Liu, M.; Chen, Y. *et al.* Controlled Growth of High-Quality Monolayer $WS_2$ Layers on Sapphire and Imaging Its Grain Boundary. *ACS Nano* **2013**, *7*, 8963–8971.

20. Bao, W.; Borys, N. J.; Ko, C.; Suh, J.; Fan, W.; Thron, A.; Zhang, Y.; Buyanin, A.; Zhang, J.; Cabrini, S. *et al.* Visualizing Nanoscale Excitonic Relaxation Properties of Disordered Edges and Grain Boundaries in Monolayer Molybdenum Disulfide. *Nature Communications* **2015**, *6*, 021001.

21. Liu, H.; Lu, J.; Ho, K.; Hu, Z.; Dang, Z.; Carvalho, A.; Tan, H. R.; Tok, E. S.; Sow, C. H. Fluorescence Concentric Triangles: A Case of Chemical Heterogeneity in $WS_2$ Atomic Monolayer. *Nano Letters* **2016**, *16*, 5559–5567.

22. Kim, M. S.; Yun, S. J.; Lee, Y.; Seo, C.; Han, G. H.; Kim, K. K.; Lee, Y. H.; Kim, J. Biexciton Emission from Edges and Grain Boundaries of Triangular $WS_2$ Monolayers. *ACS Nano* **2016**, *10*, 2399–2405.

23. Zheng, C.; Xu, Z.-Q.; Zhang, Q.; Edmonds, M. T.; Watanabe, K.; Taniguchi, T.; Bao, Q.; Fuhrer, M. S. Profound Effect of Substrate Hydroxylation and Hydration on Electronic and Optical Properties of Monolayer $MoS_2$. *Nano Letters* **2015**, *15*, 3096–3102.

24. Gao, J.; Li, B.; Tan, J.; Chow, P.; Lu, T.-M.; Koratkar, N. Aging of Transition Metal Dichalcogenide Monolayers. *ACS Nano* **2016**, *10*, 2628–2635.

25. Cong, C.; Shang, J.; Wu, X.; Cao, B.; Peimyoo, N.; Qiu, C.; Sun, L.; Yu, T. Synthesis and Optical Properties of Large-Area Single-Crystalline 2D Semiconductor $WS_2$ Monolayer from Chemical Vapor Deposition. *Advanced Optical Materials* **2013**, *2*, 131–136.

26. Peimyoo, N.; Shang, J.; Cong, C.; Shen, X.; Wu, X.; Yeow, E. K. L.; Yu, T. Nonblinking, Intense Two-Dimensional Light Emitter: Monolayer $WS_2$ Triangles. *ACS Nano* **2013**, *7*, 10985–10994.

27. Yore, A. E.; Smithe, K. K. H.; Crumrine, W.; Miller, A.; Tuck, J. A.; Redd, B.; Pop, E.; Wang, B.; Newaz, A. K. M. Visualization of Defect-Induced Excitonic Properties of the Edges and Grain Boundaries in Synthesized Monolayer Molybdenum Disulfide. *The Journal of Physical Chemistry C* **2016**, *120*, 24080–24087.

28. McCreary, K. M.; Currie, M.; Hanbicki, A. T.; Chuang, H.-J.; Jonker, B. T. Understanding Variations in Circularly Polarized Photoluminescence in Monolayer Transition Metal Dichalcogenides. *ACS Nano* **2017**, *11*, 7988–7994.

29. McCormick, E. J.; Newburger, M. J.; Luo, Y. K.; McCreary, K. M.; Singh, S.; Martin, I. B.; Cichewicz, E. J.; Jonker, B. T.; Kawakami, R. K. Imaging Spin Dynamics in Monolayer $WS_2$ by Time-Resolved Kerr Rotation Microscopy. *2D Materials* **2017**, *5*, 011010.

30. Borys, N. J.; Barnard, E. S.; Gao, S.; Yao, K.; Bao, W.; Buyanin, A.; Zhang, Y.; Tongay, S.; Ko, C.; Suh, J. *et al.* Anomalous Above-Gap Photoexcitations and Optical Signatures of Localized Charge Puddles in Monolayer Molybdenum Disulfide. *ACS Nano* **2017**, *11*, 2115–2123.

31. Sheng, Y.; Wang, X.; Fujisawa, K.; Ying, S.; Elias, A. L.; Lin, Z.; Xu, W.; Zhou, Y.; Korsunsky, A. M.; Bhaskaran, H. *et al.* Photoluminescence Segmentation within Indi-

vidual Hexagonal Monolayer Tungsten Disulfide Domains Grown by Chemical Vapor Deposition. *ACS Applied Materials & Interfaces* **2017**, *9*, 15005–15014.

32. Bogaert, K.; Liu, S.; Liu, T.; Guo, N.; Zhang, C.; Gradečak, S.; Garaj, S. Two-Dimensional $Mo_xW_{1-x}S_2$ Graded Alloys: Growth and Optical Properties. *Scientific Reports* **2018**, *8*, 12889.

33. Dhakal, K. P.; Duong, D. L.; Lee, J.; Nam, H.; Kim, M.; Kan, M.; Lee, Y. H.; Kim, J. Confocal Absorption Spectral Imaging of $MoS_2$: Optical Transitions Depending on the Atomic Thickness of Intrinsic and Chemically Doped $MoS_2$. *Nanoscale* **2014**, *6*, 13028–13035.

34. Park, S.; Kim, H.; Kim, M. S.; Han, G. H.; Kim, J. Dependence of Raman and Absorption Spectra of Stacked Bilayer $MoS_2$ on the Stacking Orientation. *Optics Express* **2016**, *24*, 21551.

35. Castellanos-Gomez, A.; Quereda, J.; van der Meulen, H. P.; AgraÃŕt, N.; Rubio-Bollinger, G. Spatially Resolved Optical Absorption Spectroscopy of Single- and Few-Layer $MoS_2$ by Hyperspectral Imaging. *Nanotechnology* **2016**, *27*, 115705.

36. Nozaki, J.; Kobayashi, Y.; Miyata, Y.; Maniwa, Y.; Watanabe, K.; Taniguchi, T.; Yanagi, K. Local Optical Absorption Spectra of h-BN–$MoS_2$ van der Waals Heterostructure Revealed by Scanning Near-Field Optical Microscopy. *Japanese Journal of Applied Physics* **2016**, *55*, 06GB01.

37. Yuan, L.; Chung, T.-F.; Kuc, A.; Wan, Y.; Xu, Y.; Chen, Y. P.; Heine, T.; Huang, L. Photocarrier generation from interlayer charge-transfer transitions in WS 2 -graphene heterostructures. *Science Advances* **2018**, *4*, e1700324.

38. Lee, J. E.; Ahn, G.; Shim, J.; Lee, Y. S.; Ryu, S. Optical Separation of Mechanical Strain from Charge Doping in Graphene. *Nature Communications* **2012**, *3*, 1024.

39. Michail, A.; Delikoukos, N.; Parthenios, J.; Galiotis, C.; Papagelis, K. Optical Detection of Strain and Doping Inhomogeneities in Single Layer $MoS_2$. *Applied Physics Letters* **2016**, *108*, 173102.

40. Rao, R.; Islam, A. E.; Singh, S.; Berry, R.; Kawakami, R. K.; Maruyama, B.; Katoch, J. Spectroscopic evaluation of charge-transfer doping and strain in graphene/ MoS2 heterostructures. *Physical Review B* **2019**, *99*, 195401.

41. Tongay, S.; Suh, J.; Ataca, C.; Fan, W.; Luce, A.; Kang, J. S.; Liu, J.; Ko, C.; Raghunathanan, R.; Zhou, J. *et al.* Defects Activated Photoluminescence in Two-Dimensional Semiconductors: Interplay between Bound, Charged and Free Excitons. *Scientific Reports* **2013**, *3*, 2657.

42. Nan, H.; Wang, Z.; Wang, W.; Liang, Z.; Lu, Y.; Chen, Q.; He, D.; Tan, P.; Miao, F.; Wang, X. *et al.* Strong Photoluminescence Enhancement of $MoS_2$ through Defect Engineering and Oxygen Bonding. *ACS Nano* **2014**, *8*, 5738–5745.

43. Chow, P. K.; Jacobs-Gedrim, R. B.; Gao, J.; Lu, T.-M.; Yu, B.; Terrones, H.; Koratkar, N. Defect-Induced Photoluminescence in Monolayer Semiconducting Transition Metal Dichalcogenides. *ACS Nano* **2015**, *9*, 1520–1527.

44. Sun, L.; Zhang, X.; Liu, F.; Shen, Y.; Fan, X.; Zheng, S.; Thong, J. T. L.; Liu, Z.; Yang, S. A.; Yang, H. Y. Vacuum Level Dependent Photoluminescence in Chemical Vapor Deposition-Grown Monolayer $MoS_2$. *Scientific Reports* **2017**, *7*, 16714.

45. Mak, K. F.; He, K.; Lee, C.; Lee, G. H.; Hone, J.; Heinz, T. F.; Shan, J. Tightly Bound Trions in Monolayer $MoS_2$. *Nature Materials* **2012**, *12*, 207–211.

46. Barja, S.; Wickenburg, S.; Liu, Z.-F.; Zhang, Y.; Ryu, H.; Ugeda, M. M.; Hussain, Z.; Shen, Z.-X.; Mo, S.-K.; Wong, E. *et al.* Charge Density Wave Order in 1D Mirror Twin Boundaries of Single-Layer $MoSe_2$. *Nature Physics* **2016**, *12*, 751–756.

47. Feng, J.; Qian, X.; Huang, C.-W.; Li, J. Strain-Engineered Artificial Atom as a Broad-Spectrum Solar Energy Funnel. *Nature Photonics* **2012**, *6*, 866–872.

48. Castellanos-Gomez, A.; Roldán, R.; Cappelluti, E.; Buscema, M.; Guinea, F.; van der Zant, H. S. J.; Steele, G. A. Local Strain Engineering in Atomically Thin $MoS_2$. *Nano Letters* **2013**, *13*, 5361–5366.

49. Zhang, Q.; Chang, Z.; Xu, G.; Wang, Z.; Zhang, Y.; Xu, Z.-Q.; Chen, S.; Bao, Q.; Liu, J. Z.; Mai, Y.-W. *et al.* Strain Relaxation of Monolayer $WS_2$ on Plastic Substrate. *Advanced Functional Materials* **2016**, *26*, 8707–8714.

50. Frisenda, R.; DrÃijppel, M.; Schmidt, R.; de Vasconcellos, S. M.; de Lara, D. P.; Bratschitsch, R.; Rohlfing, M.; Castellanos-Gomez, A. Biaxial Strain Tuning of the Optical Properties of Single-Layer Transition Metal Dichalcogenides. *npj 2D Materials and Applications* **2017**, *1*, 10.

51. Khatibi, Z.; Feierabend, M.; Selig, M.; Brem, S.; LinderÃďlv, C.; Erhart, P.; Malic, E. Impact of Strain on the Excitonic Linewidth in Transition Metal Dichalcogenides. *2D Materials* **2018**, *6*, 015015.

52. Niehues, I.; Schmidt, R.; DrÃijppel, M.; Marauhn, P.; Christiansen, D.; Selig, M.; BerghÃďuser, G.; Wigger, D.; Schneider, R.; Braasch, L. *et al.* Strain Control of Exciton–Phonon Coupling in Atomically Thin Semiconductors. *Nano Letters* **2018**, *18*, 1751–1757.

53. McCreary, K. M.; Hanbicki, A. T.; Singh, S.; Kawakami, R. K.; Jernigan, G. G.; Ishigami, M.; Ng, A.; Brintlinger, T. H.; Stroud, R. M.; Jonker, B. T. The Effect of Preparation Conditions on Raman and Photoluminescence of Monolayer $WS_2$. *Scientific Reports* **2016**, *6*, 35154.

54. McIntyre, J.; Aspnes, D. Differential Reflection Spectroscopy of Very Thin Surface Films. *Surface Science* **1971**, *24*, 417–434.

55. Chernikov, A.; Ruppert, C.; Hill, H. M.; Rigosi, A. F.; Heinz, T. F. Population Inversion and Giant Bandgap Renormalization in Atomically Thin $WS_2$ Layers. *Nature Photonics* **2015**, *9*, 466–470.

56. Kozawa, D.; Kumar, R.; Carvalho, A.; Amara, K. K.; Zhao, W.; Wang, S.; Toh, M.; Ribeiro, R. M.; Neto, A. H. C.; Matsuda, K. *et al.* Photocarrier Relaxation Pathway in Two-Dimensional Semiconducting Transition Metal Dichalcogenides. *Nature Communications* **2014**, *5*, 4543.

57. Mouri, S.; Miyauchi, Y.; Matsuda, K. Tunable Photoluminescence of Monolayer MoS2 via Chemical Doping. *Nano Letters* **2013**, *13*, 5944–5948.

58. Yang, F.; Wilkinson, M.; Austin, E. J.; O'Donnell, K. P. Origin of the Stokes Shift: A Geometrical Model of Exciton Spectra in 2D Semiconductors. *Physical Review Letters* **1993**, *70*, 323–326.

59. Valkovskii, V.; Jandieri, K.; Gebhard, F.; Baranovskii, S. D. Rethinking the Theoretical Description of Photoluminescence in Compound Semiconductors. *Journal of Applied Physics* **2018**, *123*, 055703.

60. Schmitt-Rink, S.; Chemla, D.; Miller, D. Linear and Nonlinear Optical Properties of Semiconductor Quantum Wells. *Advances in Physics* **1989**, *38*, 89–188.

61. Hawrylak, P. Optical Properties of a Two-Dimensional Electron Gas: Evolution of Spectra from Excitons to Fermi-Edge Singularities. *Physical Review B* **1991**, *44*, 3821–3828.

62. AıÌĹt-Ouali, A.; Yip, R. Y.-F.; Brebner, J. L.; Masut, R. A. Strain Relaxation and Exciton Localization Effects on the Stokes Shift in $InAs_xP_{1-x}$/InP Multiple Quantum Wells. *Journal of Applied Physics* **1998**, *83*, 3153–3160.

63. He, K.; Poole, C.; Mak, K. F.; Shan, J. Experimental Demonstration of Continuous

Electronic Structure Tuning via Strain in Atomically Thin MoS2. *Nano Letters* **2013**, *13*, 2931–2936.

64. Absor, M. A. U.; Kotaka, H.; Ishii, F.; Saito, M. Strain-Controlled Spin Splitting in the Conduction Band of monolayer$WS_2$. *Physical Review B* **2016**, *94*, 115131.

65. Liu, G.-B.; Shan, W.-Y.; Yao, Y.; Yao, W.; Xiao, D. Three-Band Tight-Binding Model for Monolayers of Group-VIB Transition Metal Dichalcogenides. *Physical Review B* **2013**, *88*, 085433.

66. Guo, S.; Zheng, H.; Wang, Y.; Zhang, J. Achieving giant spin-orbit splitting in conduction band of monolayer WS2 via n-p co-doping. *AIP Advances* **2019**, *9*, 075304.

67. Romanov, A. E.; Beltz, G. E.; Speck, J. S. Crack formation in surface layers with strain gradients. *International Journal of Materials Research* **2007**, *98*, 723–728.

68. Wang, X.; Tabarraei, A.; Spearot, D. E. Fracture mechanics of monolayer molybdenum disulfide. *Nanotechnology* **2015**, *26*, 175703.

69. lin Xiong, Q.; huan Li, Z.; geng Tian, X. Fracture behaviors of pre-cracked monolayer molybdenum disulfide: A molecular dynamics study. *Beilstein Journal of Nanotechnology* **2016**, *7*, 1411–1420.

70. Krustok, J.; Kaupmees, R.; Jaaniso, R.; Kiisk, V.; Sildos, I.; Li, B.; Gong, Y. Local Strain-Induced Band Gap Fluctuations and Exciton Localization in Aged $WS_2$ Monolayers. *AIP Advances* **2017**, *7*, 065005.

71. Zhang, Q.; Lu, J.; Wang, Z.; Dai, Z.; Zhang, Y.; Huang, F.; Bao, Q.; Duan, W.; Fuhrer, M. S.; Zheng, C. Reliable Synthesis of Large-Area Monolayer $WS_2$ Single Crystals, Films, and Heterostructures with Extraordinary Photoluminescence Induced by Water Intercalation. *Advanced Optical Materials* **2018**, *6*, 1701347.

# Graphical TOC Entry

